An Ultra-Low Power PPG and mm-Resolution ToF PPD-Based CMOS Chip Towards All-in-One Photonic Sensors

Assim Boukhayma, *Member, IEEE*, Antonino Caizzone, *Member, IEEE*, and Christian Enz, *Fellow, IEEE*

***Abstract*— This paper presents a CMOS photonic sensor covering multiple applications from ambient light sensing to time resolved photonic sensing. The sensor is made of an array of gated pinned photodiodes (PPDs) averaged using binning and passive switched-capacitor (SC) charge sharing combined with ultra-low-power amplification and analog-to-digital conversion. The chip is implemented in a 180 nm CMOS image sensor (CIS) process and features high sensitivity, low-noise and low-power performance. Measurement results demonstrate μW health monitoring through Photoplethysmography (PPG), 10 ps resolution for time resolved light sensing and mm precision for time-of-flight (ToF) distance ranging obtained with a frame rate of 50 Hz and 20 dB ambient light rejection.**

***Index Terms*— PPD, PPG, single-point ToF, time resolved, ultra-low-power, CMOS, sensor.**

I. Introduction

IN THE ever expending field of consumer electronics and wearable devices, light sensing is playing a key role in closing the loop between the user, his environment and the electronic device. Devices such as smartphones, smartwatches or wrist bands embed photonic sensors for imaging, display control, user recognition, proximity sensing and even health monitoring involving measurements of the light intensity, photons time-of-flight (ToF) or spectroscopy.

Increasing the interest for portable consumer electronics relays on two conflicting factors which are miniaturization and battery lifetime on one side, and enhancing the applications and interaction possibilities on the other side. Hence, integrating more and more sensors is becoming one of the key challenges in the smartphone and smartwatch industry especially for photonic sensors that require specific constraints such us being all located at the surface of the device.

One question rises when addressing this problem, would it be possible to converge several photonic applications in a single sensor? The move of some semiconductor market leaders towards this direction supports the relevance of this question [1]. One of the challenges facing this all-in-one trend resides at the early front-end of each light sensing readout chain: the photosensitive device. Indeed, today large junction photodiodes are used for ambient light sensing (ALS) [2], CMOS pinned photodiodes (PPDs) are used for imaging [3], single photon avalanche photodiodes (SPADs) are used for direct ToF [4] and so on. Each type of these sensors derives from a different mainstream technology making it complicated to integrate on a same chip.

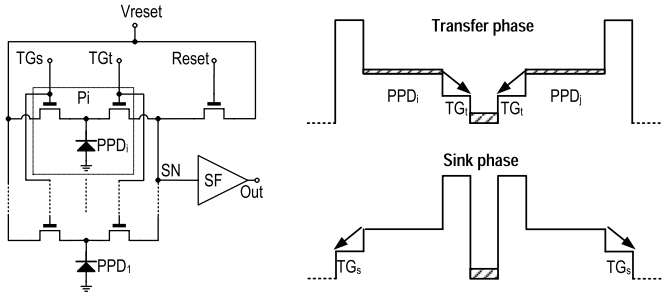

Fig. 1. Macro-pixel architecture and charge binning working principle.

Nonetheless, the pinned photodiode (PPD) [5] presents a great opportunity in this regard. PPDs are perfectly integrated into CMOS processe with even advanced technology nodes [6] [7]. The performance features proven in the last decade at the level of noise, sensitivity and dynamic range make PPDs ultimately suitable for high precision light sensing [8]–[11]. In addition, the fast gating of these devices offers the possibility of addressing time resolved applications such as ToF [13]–[16]. Last but not least, the compatibility of PPDs with CMOS processes [6] reduces dramatically the cost for large volume production.

In this paper, we propose an answer to the question raised above. A PPD based sensor chip suitable for a variety of applications related to mobile and wearable devices and key features such as ultra-low power, high sensitivity and ultra-low noise.Most PPD based sensors presented in the litterature are targetting imaging applications like photography or depth mapping. This work exploite PPDs for single-point light sensing by immplementing a dedicated architecture trading spacial resolution for power consumption and precision. The proposed PPD based sensor performance is demonstrated, evaluated and compared to current state of the art (SOA), for two emerging applications which are single-point ToF for distance measurement and Photoplethysmography (PPG) for health monitoring. Part of the results related to the PPG application using this sensor have been recently presented in [17]. An extension of these results is also provided.

Manuscript received June 24, 2019; revised August 29, 2019; accepted September 2, 2019. Date of publication September 4, 2019; date of current version November 26, 2019. The associate editor coordinating the review of this article and approving it for publication was Prof. Takashi Tokuda. *(Assim Boukhayma and Antonino Caizzone contributed equally to this work.) (Corresponding author: Assim Boukhayma.)*

The authors are with the ICLAB, École Polytechnique Fédérale de Lausanne, 2000 Neuchâtel, Switzerland (e-mail: assim.boukhayma@epfl.ch; antonino.caizzone@epfl.ch; chrisitan.enz@epfl.ch).

Digital Object Identifier 10.1109/JSEN.2019.2939479

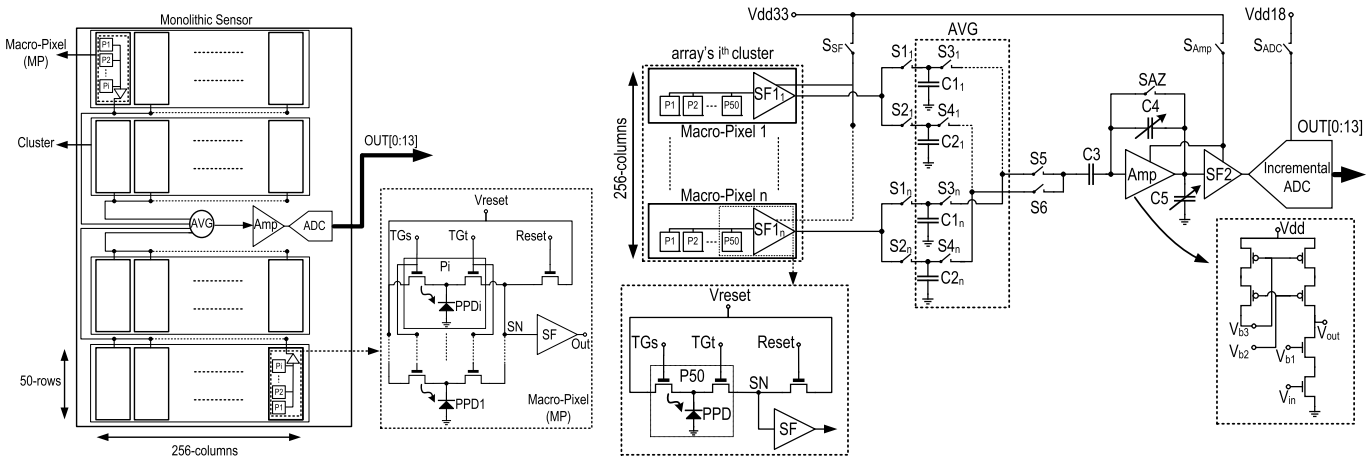

Fig. 2. The PPD-based sensor: (a) block diagram of the proposed sensor and (b) architecture of the sensor and detailed schematic of the OTA, used in the amplifier, and the averaging block.

This paper is organized as follows: Section II presents the global architecture of the sensor chip, Section III presents a general characterization of the sensor for light sensing, Section IV demonstrates the pertinence of the sensor for PPG and Section V demonstrates its performance for time resolved applications and ToF distance measurements in particular. Section VI discusses the general performance of the sensor and compares it to the current SOA before conclusion.

II. The PPD-Based Sensor

The sensor presented in this work is based on an array of PPDs structured in macro-pixels. Fig. 1 shows the macropixel design and the charge binning working principle. The macropixel consists of an array of PPDs having each two transfer gates (TG), a sink TG_s and a transfer gate TG_t. TG_s sinks the charge cumulated in the PPDs to the reset voltage (V_{RST}), while TG_t allows the charge transfer to the sense node (SN). The SN is shared between multiple PPDs, which are gated to either sink or transfer their charge synchronously. This process is also referred to as charge binning. It allows averaging the outputs of the macropixel PPDs without the need for any additional circuitry. This charge binning presents key advantages when compared to the implementation of a single photodiode as large as the macropixel. Indeed, PPDs may suffer from charge transfer inefficiency due to the slow diffusion charge transfer mechanism or to the presence of a potential barrier under the transfer gate [18]. These non-idealities scale with the size of the photodiode. Hence, such a combination of pixels enables more efficient and faster charge transfer compared to a single large PPD with equivalent area by mitigating the effect of charge transfer non-idealities. This aspect is particularly crucial for applications requiring fast gating such as ToF.

Fig. 2(a) shows the readout chain architecture embedding an array of the proposed macro-pixels shown in Fig. 1. Fig. 2(b) shows the full analog-front-end (AFE). The macro-pixels embed 50 double-gated PPDs organized in clusters of 256 macro-pixels. The sensor embeds 4 clusters. The number of PPDs involved in the sensor is chosen based on the most constraining targeted application in terms of dynamic range which is PPG. A medical PPG signal requires at minimum 225 million photo-electrons [19]. The number of pixels is then chosen to make the array capable of accumulating this charge when distributed on the full array avoiding the saturation of the PPD wells and the sense nodes.

At the output of each macro-pixel voltage buffer, two passive switched capacitor (SC) sample and holds are used in the following way: first, the macro-pixels SNs voltages obtained after reset or ambient light sensing are sampled and held in capacitors $C1_{1...n}$ by closing and opening switches $S1_{1...n}$. Second, in the same way, the SNs voltages obtained after the signal transfer are sampled an held on capacitors $C2_{1...n}$ by means of switches $S2_{1...n}$. Third, the macro-pixels first and second output samples are averaged over the whole array using a process of charge sharing between capacitors $C1_{1...n}$ by closing switches $S3_{1...n}$ and capacitors $C2_{1...n}$ by closing $S4_{1...n}$.

Those two voltage averages are then fed to a variable gain SC amplifier using switches S5 and S6. S5 is closed during the amplifier autozero while S6 is closed after. In this way, the offset of SC amplifier is canceled, the low frequency noise is mitigated and the first and second array averages mentioned above are subtracted. This subtraction allows ambient light cancellation in the case of active light sensing applications as will be further detailed in the following sections.

The readout chain ends with an incremental ADC made of a delta-sigma modulator block concatenated with a ripple counter capable of delivering a variable resolution proportional to the conversion time.

Fig. 3 shows the die micrograph. The sensor is fabricated in a 180 nm CIS process. The array of macro-pixel clusters and SC network is covering an area of 2.9 mm by 2.5 mm dominating the one covered by the amplifier and ADC. No micro-lens or color filter array post processing have been added and in all experimental work detailed in the following,

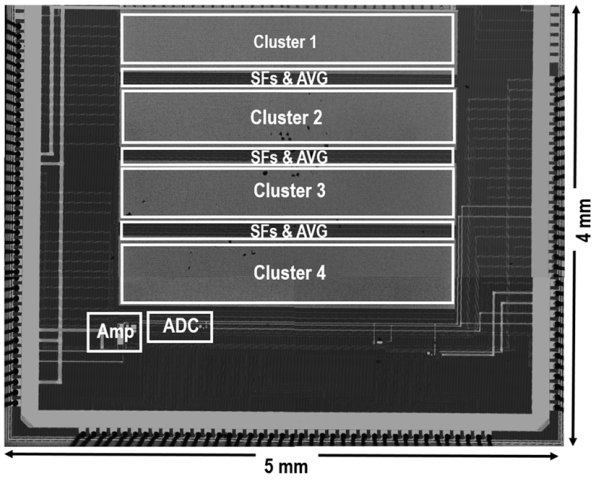

Fig. 3. Chip micrograph.

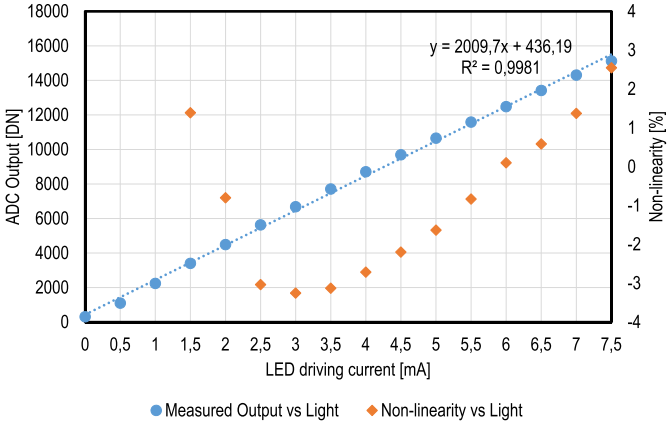

Fig. 4. Measured chip light-to-digital conversion linearity.

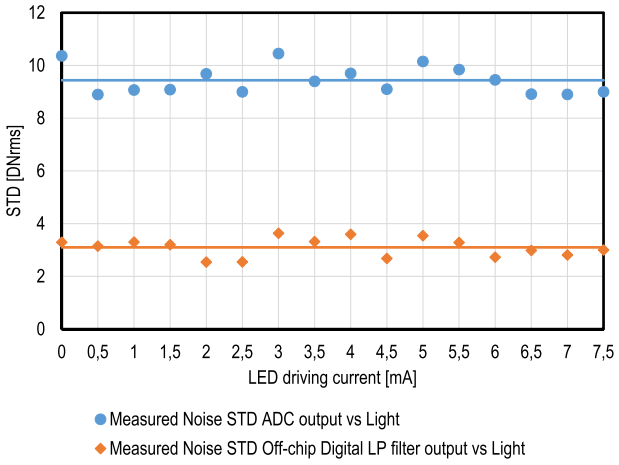

Fig. 5. Total noise STD shown both at the output of the ADC and an off-chip digital low-pass filter.

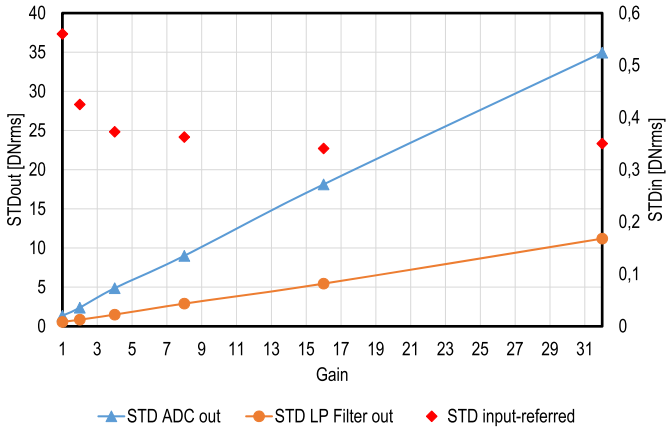

Fig. 6. Total noise STD, reported both at the output and input-referred, as a function of the gain.

the sensor chip is directly exposed to active light without any lenses or optical filters.

III. Light Sensing and Noise Performance

Before addressing PPG and ToF applications. The sensor chip performance for light sensing is first characterized. The linearity of the light to digital conversion for the proposed chip is shown in Fig. 4. This measurement is obtained by exposing the sensor to an LED shining at an increasing driving current. The ADC resolution is set to 14 bit, the integration time is set to 140 μs and the programmable amplifier gain is set to 8, enabling a wide range of emitting light conditions without saturating the read-out chain. The chip shows $\pm 3\%$ non-linearity in the light to digital conversion, with the exception of sub-mA LED input current case. Note that this includes all the sources of non-linearity from the LED, the readout chain to the ADC. On the other hand, the system is usually operated so to work around half of the full dynamic, which means, with respect to Fig. 4, keeping the ADC output around 7000 DN. In this condition, the non-linearity is less than $\pm 1\%$.

Fig. 5 shows the overall sensor's output noise standard deviation (STD). For the same experimental set-up as above, the noise STD remains constant independently of the input light. This is due to the fact that the sensor operates with an input light level low enough to let the contribution of the read noise dominate. An off-chip digital low pass filter (LPF) is used optionally to exploit the noise shaping effect of the incremental ADC. The total noise measured at the output of the LPF is $3.1\text{DN}_{\text{rms}}$ in average corresponding to 35 μV_{rms} at the level of the SNs. This noise level is equivalent to an input-referred photoelectrons charge as low as 0.68 e^-_{rms} per PPD. This is achieved thanks to the noise shaping introduced by the incremental ADC. The noise measured directly at the output of the ADC corresponds to $9.43\text{DN}_{\text{rms}}$, this accounts for all the noise components of the chain including the readout noise, quantization noise, shot noise and LED flicker noise.

Fig. 6 shows the impact of the variable analog gain on the overall noise. The output noise STD is reported at the output of the ADC as well as the off-chip digital LPF. The noise obtained at the output of the LPF is referred to the input after normalization with the analog gain. Fig. 6 shows that the noise decreases gradually by increasing the gain before reaching a plateau. The plateau represents the noise contribution level of the array and SC circuits preceding the amplifier. The

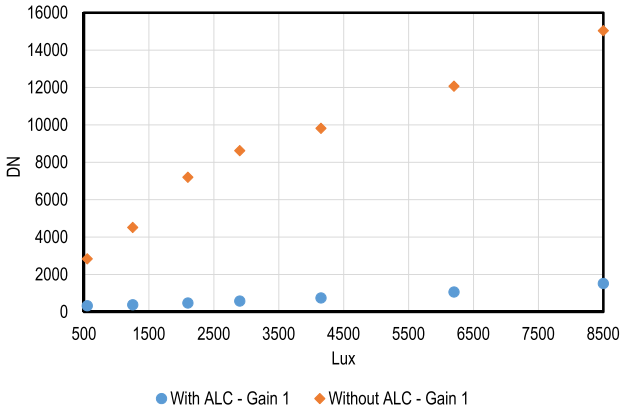

Fig. 7. Output DN with and without the ALC vs the AL.

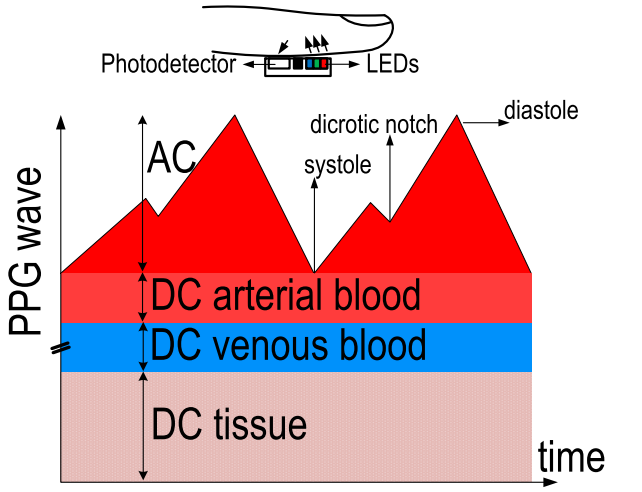

Fig. 8. PPG set-up and optical signal, highlighting the DC and AC components.

contribution of the amplifier and ADC dominates only when an analog gain below 8 is applied.

For active sensing applications such as ToF or PPG, not only light sensing is important but ambient light cancellation (ALC) is important as well. As it is described in the previous section, two consecutive samples can be sensed by the PPDs and subtracted thanks to the SC network and amplifier autozeroing. Assuming the ambient light conditions to be static during the sampling interval of 140 μs, the fist sample can sense the ambient light and the second one can have the signal superimposed on the same ambient light level. Hence the subtraction of the two samples would lead to ALC.

Fig. 7 shows the sensor performance for ALC. The sensor is exposed to varying lighting conditions from 500 to 8500 Lux. The sensor is then operated in two modes: ALS and ALC. The chip outputs in each mode are both plotted in Fig. 7. The figure shows that the sensor chip, when operating in ALC mode, reduces considerably the background light by about 20 dB with respect to the ALS mode. Note that the light source used in the experiment oscillates at 50 Hz.

IV. PPG Sensor

Photoplethysmography (PPG) allows non-invasive and efficient monitoring of several vital signs such as heart rate (HR), oxygen saturation (SpO_2), blood pressure and atrial-fibrillation. A PPG signal is obtained by shining light from an LED into a perfused tissue. The light reflected from the tissue is measured by a photodetector (PD). The detected PPG signal consists of two different components: a large DC (quasi-static) component corresponding to the light diffusion through tissues and non-pulsatile blood layers, and a small AC (pulsatile) part due to the diffusion through the arterial blood, as shown in Fig. 8. The AC/DC ratio, also called Perfusion-Index (PI), ranges typically between 0.2% and 2%. Such a small value represents one of the challenges behind the PPG technique [20].

Today, almost all the fitness trackers or smartwatches embed a PPG sensor, mostly for HR monitoring. Nevertheless, a continuous PPG monitoring is still challenging due to the dominating LED power consumption. Different solutions have been proposed to face this challenge, either by duty-cycling the LED driver at uniform sampling [19], [21] or by compressive sampling [22]. The recent work in [23] presents a heart-beat-locked loop system that significantly reduces the LED power, despite this comes at the cost of more system complexity. Indeed, the proposed solution requires a non-trivial heart beat prediction scheme and intrinsically hinders the full PPG wave representation.

The chip shown in Fig. 2 and explained in Section II is an excellent candidate as a PPG sensor. The high sensitivity photo-detecting scheme combined with an ultra-low noise and low-power readout chain can efficiently address the LED power issue. Even more important, the significant LED power reduction doesn't compromise the signal-to-noise ratio (SNR) when compared to conventional solutions. Indeed, full integration of PPDs with low SN capacitance dramatically reduces the read noise [24]. Moreover, the proposed approach also provides higher miniaturization and lower cost compared to traditional solutions with off-chip photodiodes. The use of an array additionally enables spatial averaging leading to further noise reduction. Consequently, the chip in Fig. 2 can measure a PPG signal at 1.38 bpm HR average error versus a gold-standard, at 4.6μW total power consumption, including 1.97μW LED power.

Fig. 9 shows how the circuit of Fig. 2(b) is driven to perform an efficient PPG measurement. As in Fig. 9, at first the shared SNs are reset. Immediately after, each PPD of the array starts integrating the impinging light corresponding to the ambient light (AL). The double-TG, i.e. TG_t and TG_s, structure allows to precisely control the charge integration. Indeed, before any integration the PPDs are first emptied by means of the sink switch TG_s. Once the first integration is completed, the generated photoelectrons are transferred to the SNs thanks to the transfer gates TG_t. The macro-pixel structure, as explained in Section II, performs the charge averaging at the level of the shared SN. At the end of the first transfer, the SF output voltages are sampled on capacitors $C1_{1...n}$, by opening $S1_{1...n}$.

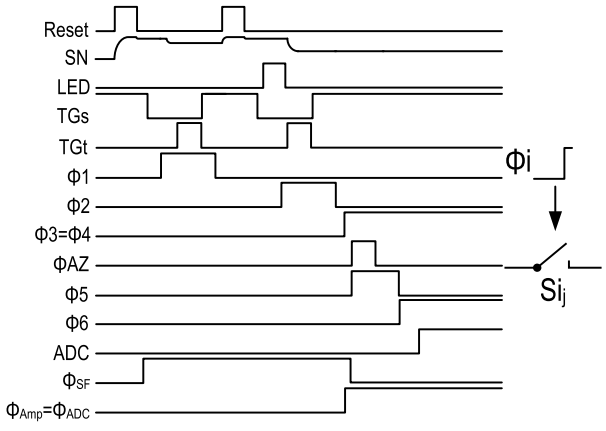

Fig. 9. PPG timing diagram related to Fig. 2(b).

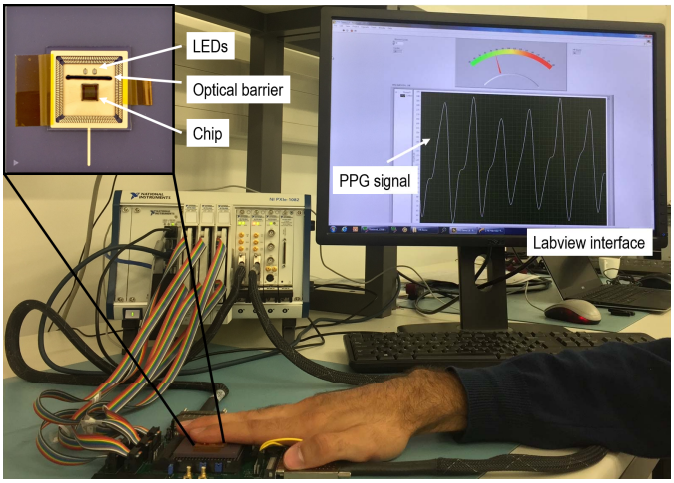

Fig. 10. PPG measurement set-up showing the sensor and the labview interface displaying the real time recorded PPG signal.

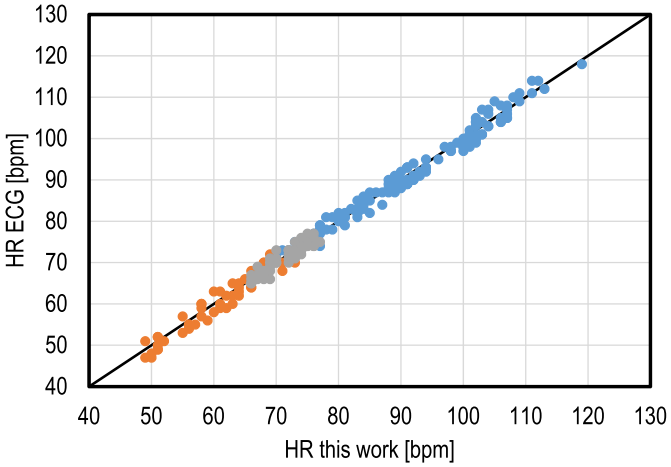

Fig. 11. Corelation of HR data between this work and a commercial ECG chest strap. The experiment has been carried out at 4.6μW total power (LED+AFE+ADC).

TABLE I
PPG SENSOR PERFORMANCE

Parameter	Value
Process	180 nm CIS
Voltage supply	3.3/1.8 V
Sampling frequency	40 Hz
LED duty cycle	0.07 %
ADC resolution	12 bits
Monolithic chip	Yes
Avg HR error	1.38 bpm
Max HR error	3 bpm
LED power	1.97 μW
AFE+ADC power	2.63 μW
TOT power	4.6 μW

In the next phase, the LED is pulsed on. Please notice that in this phase the impinging light on the sensor consists of the reflected-LED light (RLED) superimposed on the AL. As above, the SNs are first reset. At the end of this second integration the SF output voltages are sampled on capacitors $C2_{1...n}$, by opening $S2_{1...n}$. The power switch S_{SF} is only closed during this charge transfer and sampling phase for minimal power consumption.

As above-mentioned the array enables spatial averaging, leading to further noise reduction. Once the two samples, i.e. AL and RLED plus AL, are averaged, they are subtracted using the SC amplifier as described in Fig. 2.

Fig. 10 shows the PPG measurement set-up and the sensor module used for the experiment, as well as a real-time PPG signal. The sensor module consists of the PPD-chip, RGB LEDs and an optical barrier to avoid any possible cross talk between the chip and the LEDs. The chip/LEDs distance is equal to 3 mm which guarantees a good trade-off between the LED power and the recorded PI level. Fig. 11 shows a comparison between the HR directly extracted from the sensor output and a commercial ECG chest strap. The comparison features an HR maximum and average error of 3 bpm and 1.38 bpm, respectively. This is measured on three healthy male subjects for a total of 222 recordings in reflection mode on the index finger. These measurements are obtained with a sampling frequency of 40 Hz, an average LED driving power of 1.97 μW, at a duty cycle of 0.07%, and a readout (AFE+ADC) average power consumption of 2.63 μW only. This is obtained, referring to Fig. 2(b), by closing S_{SF} for 80 μs and S_{Amp} with S_{ADC} for 0.5ms. The chip performance for the PPG sensing is summarized in Table I.

V. ToF Sensor

1D ToF distance ranging is key in several applications from consumer electronics to industrial metrology. For portable applications such as drones, cameras and smartphones, safety and power consumption constraints make ToF sensors suffer from a generally poor signal reflected back from the scene featuring a small contrast with ambient light.

This section shows how the sensor presented in Section II is used to perform single point ToF distance measurement while addressing the aforementioned issues. In the following, it is demonstrated how high fill factor and ultra-low noise featured by the presented sensor enable the reduction of both

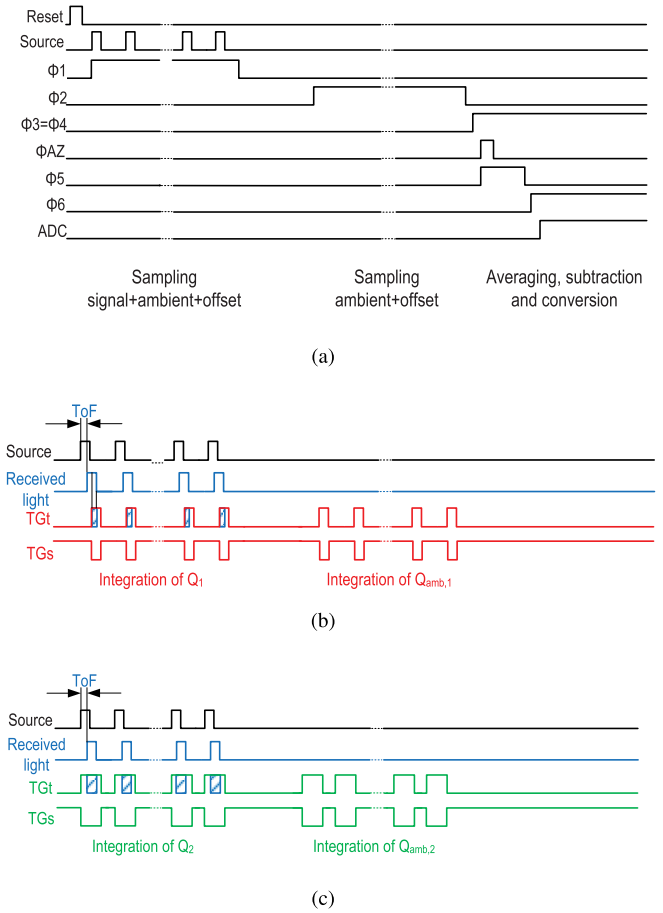

Fig. 12. PPG timing diagram related to Fig. 2(b). Readout chain (a). Transfer gates and source control for first acquisition (b) and second acquisition (c).

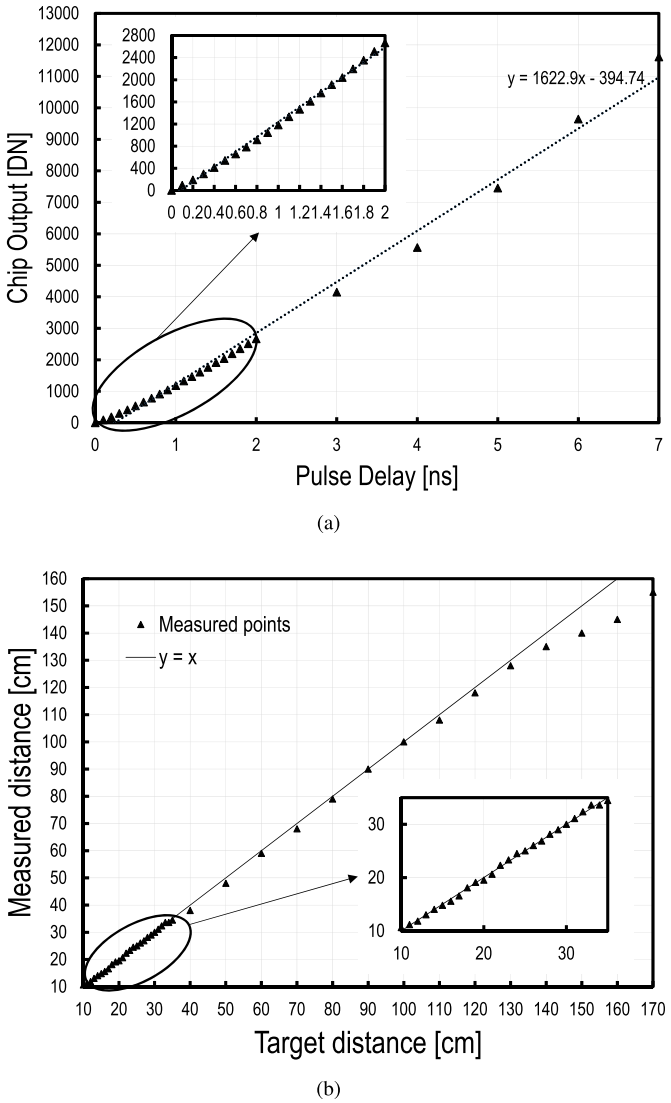

Fig. 13. Sensor output versus source pulse delay steps of 100 ps up to 2 ns and 1 ns after (a) with a zoom onto the 100 ps steps. The target versus measured distance with steps of 1 cm up to 35 cm and 1 cm after (b) measured with the sensor chip and light emitted from a VCSEL and reflected back from the target.

the light source and sensor power consumption to cope with the constraints of portable applications.

Fig. 12 shows how the circuit of Fig. 2(b) is driven to perform an indirect ToF measurement. As shown in Fig. 12(b) and Fig. 12(c), the source is modulated at the same frequency as the TG_s and TG_t. The readout operation as shown in Fig. 12(a) is repeated twice.

For the first readout, the TG_s and TG_t are operated as shown in Fig. 12(b). At the end of the phase Φ_1 a first voltage proportional to a charge Q_1 is sampled and held in capacitors $C1_{1...n}$. The charge Q_1 can be expressed roughly as

$$Q_1 = \alpha \cdot ToF \cdot Q + Q_{amb,1} + cte, \tag{1}$$

where Q is the charge corresponding to the total light emitted by the source, α is the attenuation depending on the distance and reflectivity of the object, $Q_{amb,1}$ is the charge corresponding to the ambient light and ToF is the time that light needs to travel from the source to the sensor. Indeed, the longer ToF the more emitted light gets integrated within the exposure windows. In the phase Φ_2, the same operation is repeated without pulsing on the source in order to integrate only the charge related to ambient light $Q_{amb,1}$. A voltage proportional to this charge is sampled and held on capacitors $C2_{1...n}$. Thanks to the switched capacitor amplifier, the two samples are subtracted, leading to a first sample proportional to $Q_1 - Q_{amb,1}$.

A second readout is then performed with TG_s and TG_t operated as shown in Fig. 12(c). At the end of the phase Φ_1, a first voltage proportional to a charge Q_2 is sampled and held in capacitors $C1_{1...n}$. The charge Q_2 can be expressed roughly as

$$Q_2 = \alpha \cdot Q + Q_{amb,2} + cte, \tag{2}$$

where $Q_{amb,2}$ is the charge corresponding to the ambient light. Indeed, in this phase, the integration window is large enough to integrate the total amount of charge $\alpha \times Q$. In the phase Φ_2 the same operation is repeated without pulsing on the source in order to integrate only the charge related to ambient light $Q_{amb,2}$. In the same way as above the two

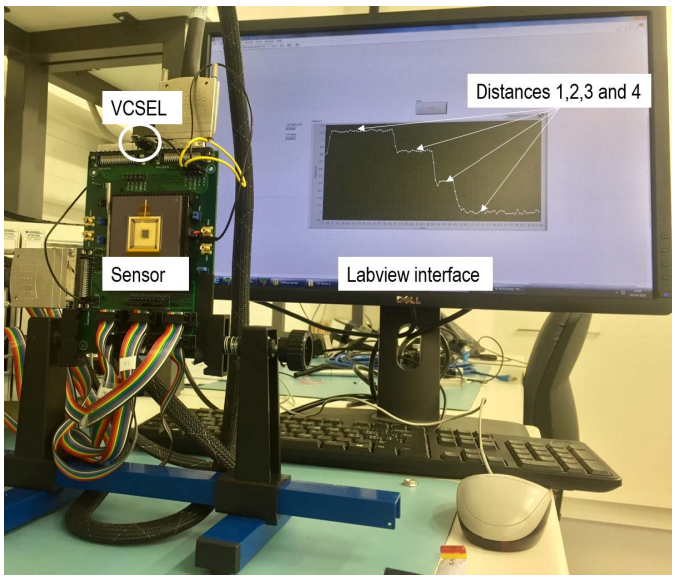

Fig. 14. ToF measurement setup showing the sensor and the VCSEL without any lenses and the labview interface displaying the real time measured distance

TABLE II
TOF SENSOR PERFORMANCE

Parameter	Value
Process	180 nm CIS
Voltage supply	3.3/1.8 V
Array size	256(H) × 4(V)
Pixel size	10 μm by 500 μm
Frame Rate	500 Hz
ADC resolution	14 bits
Integration time	640 μs with a 2 mA current supply VCSEL
Fill factor	80%
Repetition Frequency	12.5 MHz
Emitter	650 nm VCSEL
Sensor current consumption	3 μA
Emitter current consumption	2 mA
Optical setup	No lenses for emitter and sensor
Measurable range	1.7 m
Range resolution	2 mm @50Hz

samples are subtracted leading to a second sample proportional to $Q_2 - Q_{amb,2}$.

Thanks to the two separated readouts the ToF can be calculated as

$$ToF = \frac{Q_1 - Q_{amb,1}}{Q_2 - Q_{amb,2}} + cte, \tag{3}$$

where cte is a calibration parameter depending on the offset and time windows characteristics. The ratio used to calculate ToF is a normalization which makes the ToF measure insensitive to the source power.

In order to demonstrate the pertinence of the sensor for time-resolved applications, it is directly exposed to a VCSEL without any intermediate optical system. All the measurements have been performed at room temperature. The source is duty cycled to generate, during the exposure time of 6 μs, 144 consecutive pulses of 16 ns duration with a period of 40 ns as shown in Fig. 12(b) and Fig. 12(c). The average (accounting for the duty cycle) current consumption during the exposure is as small as 6 μA with a driving voltage of 2.1 V. The delay between the source pulses and the transfer windows is swept in order to characterize the way the output of the sensor follows the laser pulse delay. Fig. 13(a) shows how linearly the sensor output follows the delay generated first in steps of 100 ps and then is steps of 1 ns. The cumulative measured error standard deviation accounting for non-linearity, noise and source noise is less than 10 ps. This demonstrates that this architecture is suitable for time-resolved applications requiring 10 ps timing resolution without having to use any on-chip or off-chip high speed circuits. Applications like fluorescence lifetime imaging can strongly benefit from such a timing resolution.

With less than 10 ps timing resolution, the sensor is expected to be capable of achieving mm distance resolution in a ToF setup. A demonstrator including only the designed chip and a 10 mW 650 nm VCSEL is used to show the pertinence of this solution for applications requiring low-power, low-cost and low optical setup complexity. Fig. 14 shows the ToF measurement setup as well as the labview interface used for computing the ratio given by (3) and displaying the measured distance. The VCSEL is oriented towards the scene as well as the sensor without any focusing lenses or light filters. Only a small fraction of the VCSEL pulse light gets reflected back to the sensor from the target. The sensor is set for an exposure of 640 μs during which the VCSEL emits pulses of 16 ns with a frequency of 12.5 MHz while the transfer windows last for 40 ns following the scheme shown in Fig. 12. The VCSEL average current consumption during the exposure is less than 2 mA. The target is then moved away from the sensor and VCSEL with steps of 1 cm up to 35 cm and then with steps of 10 cm up to 170 cm. The two ambient-light-free samples corresponding to Q_1 and Q_2, as shown in Fig. 12, are processed and converted to a digital signal on-chip. The ratio of the two samples and the extraction of the measured distance thanks to a linear fit obtained with a first calibration is calculated off-chip. Fig. 13(b) shows the measured versus target distance when sweeping the target from 10 to 170 cm under an ambient light level of 3000 lux and averaging 10 consecutive frames to mitigate the set-up noise. Since the sensor operates at 500 Hz, the effective measurement frame rate is 50 Hz. The inset of Fig. 13(b) shows a focus on positions between 10 and 35 cm where the sweep step is only 1 cm. By measuring the standard deviation of the difference between the measured and target distances, an RMS value of 2 mm is obtained.

VI. DISCUSSION AND COMPARISON TO STATE-OF-THE-ART

The sensor performance for the PPG application is compared versus the most recent state-of-the-art work, as shown in Table III. With respect to [22], [23] the proposed sensor achieves the lowest power consumption, up to 1 order of magnitude less. Moreover, unlike these works, the proposed solution is a fully integrated one, meaning the photosensitive

TABLE III
PPG SENSING COMPARISON TABLE

Parameter	This work	[22]	[23]
Process	180 nm CIS	180 nm CIS	180 nm CIS
Voltage supply	3.3/1.8 V	1.2 V	3.3 V
Sampling frequency	40 Hz	4 Hz	100 Hz
LED duty cycle	0.07 %	0.0125 %	0.0175 %
ADC resolution	12 bits	12 bits	8 bits
Monolithic chip	Yes	No	No
Avg HR error	1.38 bpm	NA	NA
Max HR error	3 bpm	10 bpm	2.1 bpm
LED power	1.97 μW	43 μW	16 μW
AFE+ADC power	2.63 μW	172 μW	27.4 μW
TOT power	4.6 μW	215 μW	43.4 μW

TABLE IV
TOF SENSING COMPARISON TABLE

Parameter	This work	[26]	[25]
Process	180 nm CIS	NA	NA
Pixel technology	PPD	SPAD	SPAD
Voltage supply	3.3/1.8 V	2.8 V	3.3 V
Sensor size	3×3 mm^2 without VCSEL	4.4×2.4 mm^2 with VCSEL	2.2×3.6 mm^2 with VCSEL
Frame Rate	50 Hz	33 Hz	60 Hz
ADC resolution	14 bits	8 bits	NA
Emitter and sensor average consumption	2 mA	19 mA	NA
Optical setup	No lenses	with lenses	with lenses
Measurable range	130 cm	120 cm	60 cm
Range resolution	2 mm	48 mm	30 mm

area together with the AFE and the ADC. This offers a big advantage for the miniaturization of PPG sensors.

For ToF, the sensor performance is compared with two products freshly released by market leading companies active in the field of single-point light sensors [25], [26]. The comparison is summarized in Table IV. The comparison only covers single-point rangers and does not include depth mappers due to the fundamental difference between the constraints and required complexity and power budget fot the two applications. Both products used for comparison implement SPAD technology. Indeed SPADs are suitable for direct ToF or wave front detection [27], but such devices still present several design and industrialization challenges [28]. Indeed, SPADs require significant CMOS process optimization to cope with the large voltages needed for biasing the photo-diodes close to their breakdown limit. At the design level, direct ToF requires highly precise timing with jitters below 10 ps and suffers from small fill factors reducing the effective quantum efficiency. The architecture of the presented chip exploiting indirect ToF relaxes completely the timing precision constraints. Indeed a ToF system embedding this architecture operates with 40 ns of transfer time.

The high fill factor of this sensor together with the high QE of PPDs and the low noise of the readout chain enable the sensor to operate with lower integration time and lower emitter (VCSEL) light intensity. Compared to [25], [26] this sensor features one order of magnitude better precision with one order lower emitter light for more covered distance range. Indeed the sensor requires less than 2 mA average current dissipation in the VCSEL during exposure and only 10 μW power dissipation at the level of the sensor when operating at 50 Hz enabling a 2 mm resolution for 130 cm range.

VII. CONCLUSIONS

The sensor architecture presented in this paper not only offers the advantage of covering ALS, PPG and ToF using the same device, but it also brings significant performance improvement in each application field. Indeed, PPG sensing have been performed with a power consumption more than one order of magnitude lower for both the sensor and the emitter (LED). For single point ToF distance ranging, the resolution and emitter (VCSEL) power consumption are reduced by more than one order of magnitude as well.

Moreover, the presented architecture is implemented in a standard CIS process which presents a considerable advantage for large volume consumer applications and for miniaturization. The CMOS implementation allows also the integration of digital processing or machine learning for specific applications on the same die opening the way for edge computing.

This architecture represents a promising step towards all-in-one miniaturized photonic sensors.

REFERENCES

[1] STMicroelectronics. *All-in-One Proximity and Ambient Light Sensing Module*. Accessed: Jun. 20, 2019. [Online]. Available: https://www.st.com/en/mems-and-sensors/proximity-sensors.html
[2] *Ambient Light Sensors*. Accessed: Jun. 20, 2019. [Online]. Available: https://www.ti.com/sensors/specialty-sensors/ambient-light-sensors/overview.htm
[3] R. Fontaine, "Innovative technology elements for large and small pixel CIS devices," in *Proc. Int. Image Sensors Workshop*, Jun. 2013, pp. 1–4.
[4] J. Kvam. *Time of Flight: Principles, Challenges, and Performance*. Accessed: Jun. 20, 2019. [Online]. Available: https://www.st.com/content/dam/technology-tour-2017/session-1_track-4_time-of-flight-technology.pdf
[5] N. Teranishi, A. Kohono, Y. Ishihara, E. Oda, and K. Arai, "No image lag photodiode structure in the interline CCD image sensor," in *IEDM Tech. Dig.*, Dec. 1982, pp. 324–327.
[6] E. R. Fossum and D. B. Hondongwa, "A review of the pinned photodiode for CCD and CMOS image sensors," *IEEE J. Electron Devices Soc.*, vol. 2, no. 3, pp. 33–43, May 2014.
[7] STMicroelectronics. *Imaging Technologies*. Accessed: Jun. 20, 2019. [Online]. Available: https://www.st.com/content/st_com/en/about/innovation—technology/imaging.html
[8] J. Ma, D. Starkey, A. Rao, K. Odame, and E. R. Fossum, "Characterization of quanta image sensor pump-gate jots with deep sub-electron read noise," *IEEE J. Electron Devices Soc.*, vol. 3, no. 6, pp. 472–480, Nov. 2015.
[9] M.-W. Seo, S. Kawahito, K. Kagawa, and K. Yasutomi, "A 0.27e-RMS read noise 220-μV/e-conversion gain reset-gateless CMOS image sensor with 0.11-μm CIS process," *IEEE Electron Device Lett.*, vol. 36, no. 12, pp. 1344–1347, Dec. 2015.
[10] A. Boukhayma, A. Peizerat, and C. Enz, "Temporal readout noise analysis and reduction techniques for low-light CMOS image sensors," *IEEE Trans. Electron Devices*, vol. 63, no. 1, pp. 72–78, Jan. 2016.
[11] A. Boukhayma, A. Peizerat, and C. Enz, "A sub-0.5 electron read noise VGA image sensor in a standard CMOS process," *IEEE J. Solid State Circuits*, vol. 51, no. 9, pp. 2180–2191, Sep. 2016. doi: 10.1109/JSSC.2016.2579643.
[12] A. Boukhayma, *Ultra Low Noise CMOS Image Sensors*. Cham, Switzerland: Springer, 2018. doi: 10.1007/978-3-319-68774-2.

[13] S.-J. Kim, S.-W. Han, B. Kang, K. Lee, J. D. Kim, and C.-Y. Kim, "A three-dimensional time-of-flight CMOS image sensor with pinned-photodiode pixel structure," *IEEE Electron Device Lett.*, vol. 31, no. 11, pp. 1272–1274, Nov. 2010. doi: 10.1109/LED.2010.2066254.
[14] M.-W. Seo *et al.*, "A 10.8ps-time-resolution 256×512 image sensor with 2-Tap true-CDS lock-in pixels for fluorescence lifetime imaging," in *IEEE Int. Solid-State Circuits Conf. (ISSCC) Dig. Tech. Papers*, Feb. 2015, pp. 1–3.
[15] S.-M. Han, T. Takasawa, K. Yasutomi, S. Aoyama, K. Kagawa, and S. Kawahito, "A time-of-flight range image sensor with background canceling lock-in pixels based on lateral electric field charge modulation," *IEEE J. Electron Devices Soc.*, vol. 3, no. 3, pp. 267–275, May 2015.
[16] T.-H. Hsu, T. Liao, N.-A. Lee, and C. C. Hsieh, "A CMOS time-of-flight depth image sensor with in-pixel background light cancellation and phase shifting readout technique," *IEEE J. Solid-State Circuits*, vol. 53, no. 10, pp. 2898–2905, Oct. 2018.
[17] A. Caizzone, A. Boukhayma, and C. Enz, "A 2.6μW monolithic CMOS photoplethysmographic sensor operating with 2μW LED power," in *IEEE Int. Solid-State Circuits Conf. (ISSCC) Dig. Tech. Papers*, Feb. 2019, pp. 290–291.
[18] R. Capoccia, A. Boukhayma, F. Jazaeri, and C. Enz, "Compact modeling of charge transfer in pinned photodiodes for CMOS image sensors," *IEEE Trans. Electron Devices*, vol. 66, no. 1, pp. 160–168, Jan. 2019. doi: 10.1109/TED.2018.2875946.
[19] K. N. Glaros and E. M. Drakakis, "A sub-mW fully-integrated pulse oximeter front-end," *IEEE Trans. Biomed. Circuits Syst.*, vol. 7, no. 3, pp. 363–375, Jun. 2013.
[20] J. G. Webster, *Design of Pulse Oximeters*. Bristol, PA, USA: Institute of Physics, 1997.
[21] E. S. Winokur, T. O'Dwyer, and C. G. Sodini, "A low-power, dual-wavelength photoplethysmogram (PPG) SoC with static and time-varying interferer removal," *IEEE Trans. Biomed. Circuits Syst.*, vol. 9, no. 4, pp. 581–589, Aug. 2015.
[22] V. R. Pamula *et al.*, "A 172 μW compressively sampled photoplethysmographic (PPG) readout ASIC with heart rate estimation directly from compressively sampled data," *IEEE Trans. Biomed. Circuits Syst.*, vol. 11, no. 3, pp. 487–496, Jun. 2017.
[23] J. Lee, D.-H. Jang, S. Park, and S. Cho, "A low-power photoplethysmogram-based heart rate sensor using heartbeat locked loop," *IEEE Trans. Biomed. Circuits Syst.*, vol. 12, no. 6, pp. 1220–1229, Dec. 2018.
[24] A. Caizzone, A. Boukhayma, and C. Enz, "Comprehensive noise analysis in PPG read-out chains," in *Proc. Int. Conf. Noise Fluctuations (ICNF)*, Jun. 2017, pp. 1–4.
[25] *Worlds Smallest 1D Time-of-Flight. TMF8701 Datasheet*, ams AG, Premstätten, Austria, 2019.
[26] *Worlds Smallest Time-of-Flight Ranging and Gesture Detection Sensor. VL53L0X Datasheet*, STMicroelectronics, Geneva, Switzerland, 2019.
[27] E. A. G. Webster, J. A. Richardson, L. A. Grant, D. Renshaw, and R. K. Henderson, "A single-photon avalanche diode in 90-nm CMOS Imaging technology with 44% photon detection efficiency at 690 nm," *IEEE Electron Device Lett.*, vol. 33, no. 5, pp. 694–696, May 2012. doi: 10.1109/LED.2012.2187420.
[28] D. P. Palubiak and M. J. Deen, "CMOS SPADs: Design issues and research challenges for detectors, circuits, and arrays," *IEEE J. Sel. Topics Quantum Electron*, vol. 20, no. 6, pp. 409–426, Nov. 2014. doi: 10.1109/JSTQE.2014.2344034.

Assim Boukhayma (M'18) was born in Rabat, Morocco, in February 1988. He received the Ph.D. degree in ultralow noise CMOS image sensors from the École Polytechnique Fédérale de Lausanne (EPFL), Lausanne, Switzerland. He received the Springer thesis award in recognition for his Ph.D. outstanding research. He is currently a research team leader with the Integrated Circuits Laboratory, EPFL.

From 2012 to 2016, he was with the Commissariat a l'Energie Atomique (CEA-LETI), Grenoble, France, in the frame of his Ph.D. research. In 2012, he did his M.Sc. Internship at CEA-LETI on the design of a low-noise CMOS THz camera.

Antonino Caizzone was born in Milazzo, Italy, in March 1991. He received the bachelor's degree in electronic engineering from the University of Catania, Italy, in 2013, and the dual master's degree in micro and nano technologies from INPG Grenoble, France, and also from the Polytechnique of Turin, Italy, respectively, in 2015. He is currently pursuing the Ph.D. degree in ultra-low noise and low power sensors for healthcare with the École Polytechnique Fédérale de Lausanne (EPFL), under the supervision of Prof. Enz and Dr. Boukhayma.

From 2012 to 2013, he was with STMicroelectronics, Italy, as an Intern on the Design of Analog Electronics on Plastic Substrate. In 2014, he was with Georgia Tech, USA, as a Visiting Researcher in energy harvesters.

Christian Enz (F'19) received the M.S. and Ph.D. degrees in electrical engineering from the École Polytechnique Fédérale de Lausanne (EPFL), Lausanne, Switzerland, in 1984 and 1989, respectively.

In 1999, he joined the Swiss Center for Electronics and Microtechnology (CSEM), where he launched and led the RF and Analog IC Design Group. In 2000, he was the Vice President, heading the Microelectronics Department, which became the Integrated and Wireless Systems Division in 2009. In 2013, he joined EPFL as a Full Professor, where he is currently the Director of the Institute of Microengineering, Neuchâtel, Switzerland, and also the Head of the Integrated Circuits Laboratory (ICLAB), Neuchâtel. His current research interests include the very low-power analog and RC IC design and semiconductor device modeling.